Detailed assessment of low-voltage zones localization by cardiac MRI in patients with implantable devices

Running Title: Optimization strategies for scar localization using CMR in patients with ICDs

Michele Orini PhD* [1,2], Andreas Seraphim MBBS* [1,3], Adam Graham PhD [2], Anish Bhuva PhD[1,3], Ernesto Zacur PhD [4], Peter Kellman PhD[5], Richard Schilling MD MRCP FHRS [2], Ross Hunter PhD, MRCP FHRS[2], Mehul Dhinoja MRCP FHRS [2], Malcolm C. Finlay PhD[2], Syed Ahsan MD FRCP [2], Anthony W. Chow MD MRCP FHRS [2], James C. Moon MD [1,3], Pier D. Lambiase PhD FRCP FHRS# [1,2], Charlotte Manisty PhD# [1,3]

* Joint first authors, # Joint senior Authors

1: Institute of Cardiovascular Science, University College London, UK

2: Department of Cardiac Electrophysiology, Barts Heart Centre, Barts Health NHS Trust, London, United Kingdom

3: Department of Cardiovascular Imaging, Barts Heart Centre, Barts Health NHS Trust, London, United Kingdom

4: Department of Biomedical Engineering, University of Oxford, Oxford, UK.

5: National Institutes of Health, Bethesda, USA

Corresponding authors:

- Prof Pier D. Lambiase, Institute of Cardiovascular Science, 5 University St, London WC1E 6JF, Email: p.lambiase@ucl.ac.uk, +44(0)203 679 4407
- Dr Charlotte H. Manisty, Department of Cardiac Imaging, Barts Heart Centre, W Smithfield, London EC1A 7BE. Email: c.manisty@ucl.ac.uk

Sources of Funding

AB and AS are supported by doctoral research fellowships from the British Heart Foundation (FS/16/46/32187 and FS/18/83/34025). JCM, PDL, MO and CM are directly and indirectly supported by the University College London Hospitals and Barts

Hosptial NIHR Biomedical Research Centres. PL has received research grants from Boston Scientific, Medtronic and Abbott and speaker fees from Medtronic.

Abstract

Objective: To assess the performance and limitations of low-voltage zones (LVZ) localization by optimised late gadolinium enhancement cardiac magnetic resonance (LGE-CMR) scar imaging in patients with cardiac implantable electronic devices (CIEDs).

Background: Scar evaluation by LGE-CMR can assist ventricular tachycardia (VT) ablation, but challenges with electro-anatomical maps (EAMs) co-registration and presence of imaging artefacts from CIED limit accuracy.

Methods: 10 patients underwent VT ablation and pre-procedural LGE-CMR using wideband imaging. Scar was segmented from CMR pixel signal intensity (PSI) maps using commercial software (ADAS) with bespoke tools and compared to detailed EAMs (CARTO). Co-registration of EP and imaging derived scar was performed using the aorta as a fiducial marker and the impact of co-registration was determined by assessing intra/inter-observer variability and using computer simulations. Spatial smoothing was applied to assess correlation at different spatial resolutions and to reduce noise.

Results: PSI maps localized low-voltage zones (V<1.5 mV) with area under the ROC curve AUC=0.82 (0.76–0.83), sensitivity=74% (71%–77%) and specificity=78% (73%–83%) and correlated with bipolar voltage, r=-0.57 (-0.68 – -0.42) across patients. In simulations, small random shifts and rotations worsened LVZ localization in at least some cases. The use of the full aortic geometry ensured high reproducibility of LVZ localization (r>0.86 for AUC). Spatial smoothing improved localization of LVZ. Results for LVZ with V<0.5 mV were similar.

Conclusion: In patients with CIEDs, novel wideband CMR sequences and personalised co-registration strategies can localize LVZ with good accuracy and may assist VT ablation procedures.

Keywords: Cardiac mapping, Cardiovascular MRI, Scar, Ventricular tachycardia, Ablations

Condensed Abstract

Cardiac magnetic resonance (CMR) imaging has the potential to localize scar non-invasively and improve ventricular tachycardia (VT) ablation. However, artefacts due to implantable devices (CIEDs), inaccuracy in co-registration with electro-anatomical maps and noise may limit its use. We used optimized wideband sequences and image analysis to assess performance and limitations of low-voltage zones (LVZ) localization by CMR in patients with CIEDs. We found that using the thoracic aorta for co-registration provides good point-by-point correlation (r~-0.60) and good LVZ discrimination (AUC~0.80), with high intra- and inter-observer reproducibility. Spatial smoothing improved overall CMR-EAM agreement at the expense of reducing spatial resolution.

Abbreviations

VT: Ventricular Tachycardia

EAM: Electro-anatomical mapping

LGE-CMR: Late Gadolinium enhanced Cardiac Magnetic Resonance

CIED: Cardiac Implantable Electronic Device

LVZ: Low-voltage Zone

PSI: Pixel Signal Intensity

Central Figure

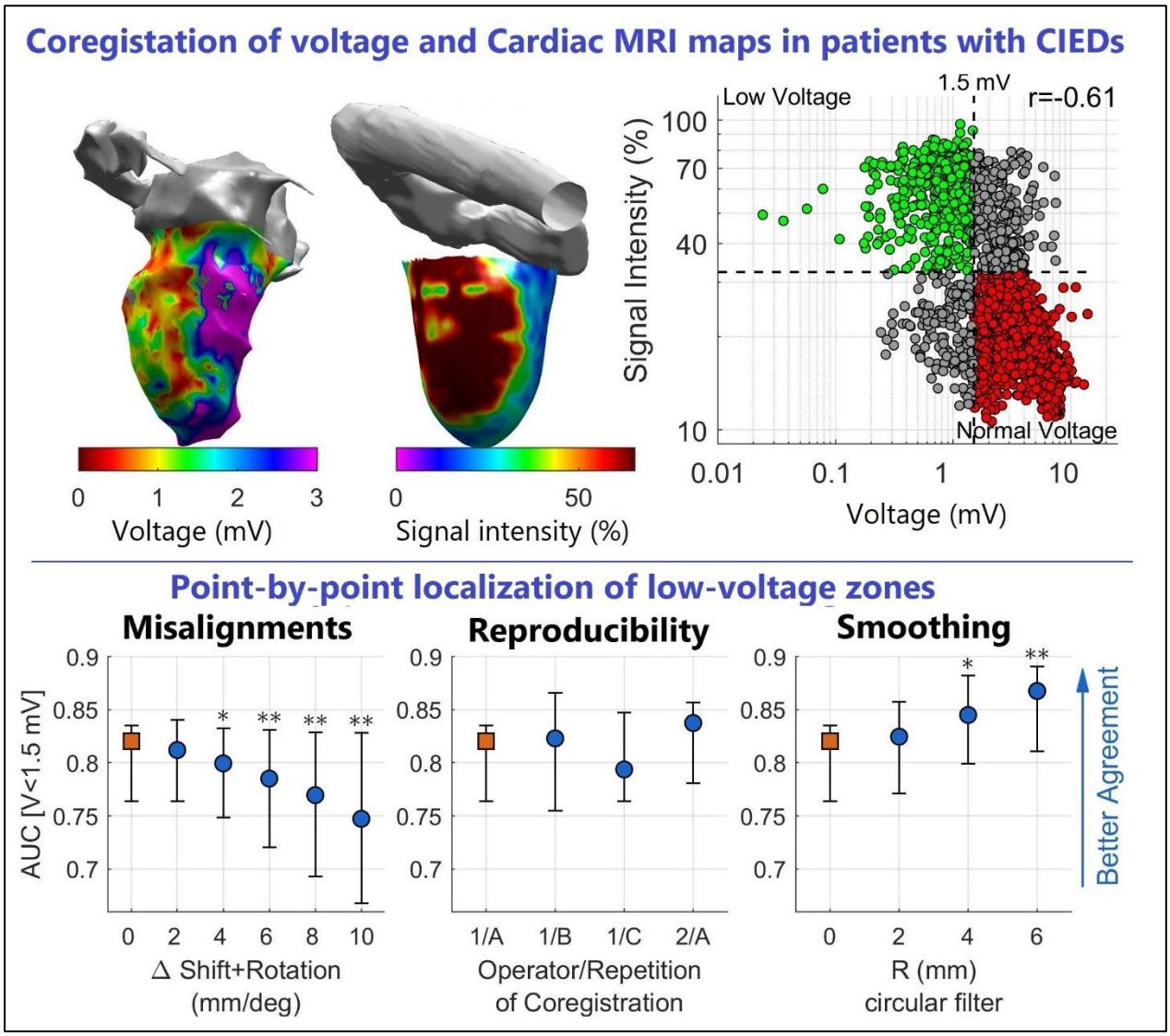

Introduction

Catheter ablation improves outcomes in patients with frequent life-threatening ventricular tachycardia (VT). However, VT recurrence rates remain unacceptably high necessitating the pursuit of more effective ablation strategies (1). Late gadolinium enhancement cardiac magnetic resonance (LGE-CMR) can provide non-invasive visualisation of arrhythmogenic substrate (2–6) and its integration with electro-anatomical mapping (EAM) can improve procedural outcomes (7–9). Indeed, recent work has proposed the utilisation of an MRI-guided approach (9), based on EAM system and CMR-derived scar co-registration. The integration of LGE-CMR scar maps and EAM for VT ablation is however not widespread. There are several reasons for this. Firstly, the precise co-registration of whole heart LGE-CMR with EAM is challenging. Secondly, most patients requiring VT ablation have cardiac implantable electronic devices (CIEDs) in-situ. Although scanning can now be performed safely with appropriate protocols (10,11), meaning almost all patients could now have LGE-CMR, the CIED itself generates image artefact (signal dropout, hyperintensity artefact) that hinders scar delineation. Dedicated sequences incorporating a wideband inversion pulse can reduce this (10), but few studies have examined feasibility of LGE-CMR and EAM co-registration in these patients (8,12,13) and the agreement in scar localization between the two modalities remains undetermined. In this study, we deploy a novel wideband LGE sequence that is fast, free-breathing and incorporates phase-sensitive inversion recovery (10). We investigate the spatial correlation between low-voltage zones from state of the art EAM and 3D CMR pixel signal intensity (PSI) maps in patients with CIEDs (10) and focused on optimal approaches for co-registration that maximise clinical utility.

Methods

Study population

The study was approved by the National Health Service Research Ethics Committee (14/LO/0360) and Health Research Authority (HRA) and was conducted in accordance with the Declaration of Helsinki. All subjects provided written, informed consent. Ten (n=10) consecutive patients (1 female, median age 75 years, interquartile range 70 – 79 years, 9 ischemic cardiomyopathy, 1 non-ischaemic dilated cardiomyopathy) with CIEDs (5 ICD, 5 CRT-D, 50% non-MR conditional) undergoing catheter VT ablation between 2017 and 2019 (8 first time, 2 repeat ablations, Table 1) were included in the analysis. Specifically, patients were included if they underwent LGE-CMR shortly before catheter ablation and if a detailed LV substrate map and a complete aortic geometry, including ascending, arch and descending aorta, were collected during the electrophysiological study. In all patients, catheter ablation was performed because of recurrent VTs and frequent ICD therapy. Five cases were elective and 5 were urgent cases for treatment of incessant VT or VT storm. Among the 9 patients with ischaemic cardiomyopathy, myocardial infarction was more frequently seen in the anterior wall (bullseye plot of scar distribution is shown in the Supplementary Material, Figure S1).

CMR protocol and data analysis

All patients underwent LGE-CMR prior to their procedure. CMR studies were performed on a 1.5T scanner (Aera, Siemens Healthineers, Erlangen, Germany) using a 30-channel phased array receiver coil, scanned at Normal Operating Mode (SAR limit <2 W/kg). In brief, device interrogation and re-programming occurred immediately before and after scanning, according to international guidelines. Patients were monitored throughout using ECG and pulse oximetry waveform assessment.

An axial stack of images through the thorax was acquired for visualisation of extracardiac structures, including the thoracic ascending and descending aorta to enable co-registration with EAM data. This used a black blood Half-Fourier Acquisition Single-shot Turbo spin Echo (HASTE) sequence, with 5mm slice thickness and zero gap between slices. Late gadolinium images were acquired 10-15 min after administration of 0.1 mmol/kg of Dotarem (Guerbet S.A.,Paris). The sequence used was a 2D motion-corrected (free-breathing) single-shot FLASH sequence with a 3.9 kHz (wideband) inversion pulse, with flip angle of 10°, phase sensitive inversion recovery (PSIR)(10) and 24 averages to recover signal to noise. Contiguous 4 mm short-axis slices were acquired with spatial resolution of 1.9x1.4 mm, which was interpolated to 1.4x1.4 mm for display and analysis. Epicardial and endocardial borders were segmented, generating a 3D pixel signal intensity map of the left ventricle (LV) using custom software (ADAS-VT, Galgo Medical, Spain) (6–8) . Nine concentric surface layers from sub-endocardium (10% of wall thickness) to sub-epicardium (90% of wall thickness) were created automatically. Subsequently, pixel signal intensity (PSI) maps were projected over each LV layer using a trilinear interpolation and color-coding to visualize PSI distribution. PSI was normalized, with global minimum and maximum across all layers set equal to 0 and 100, respectively. A tool in the same software was also used to create a 3D surface representation of the aorta from the 2D axial anatomical images and to co-register this with the LV PSI map.

EAM protocol and data analysis

Procedures were performed under conscious sedation using diamorphine and midazolam, or general anaesthetic. Vascular access was obtained under ultrasound guidance using Seldinger technique via the right femoral vein and/or right femoral

artery. The LV was accessed retrogradely via the aorta in all cases. Trans-septal puncture was additionally performed in 4 cases to gain better overall access and mapping coverage of the LV. A full geometry of the ascending, arch, and descending aorta was created for co-registration with CMR-LGE scar meshes. Collection of this geometry took less than 5 minutes in each case. A voltage map was created using a multipolar catheter (Pentaray, CARTO, Biosense-Webster, CA), and the ST SF Thermocool ablation catheter was also used in some cases. Most of intracardiac mapping was performed continuously with criteria for collecting data including close tissue proximity (using Tissue Proximity Indicator for Pentaray), position stability and contact force within 2-40 g (when using the ablation catheter). Occasionally, data collection was performed manually. EAM generated using less than 100 electrode points were excluded.

CARTO generated meshes describing the spatial distribution of bipolar voltage of the LV endocardium were exported for off-line analysis. Bipolar voltage <1.5 mV and <0.5 mV was considered indicative of scar and dense scar, respectively.

EAM-CMR comparison

PSI color-coded maps were not visible to operators during the electrophysiological study to reduce potential biases and co-registration of EAM and CMR geometries was performed retrospectively (after each case) using bespoke software (Matlab, The Mathworks, Inc, MA) (14,15) that allows the operator to move and rotate EAM and CMR geometries and inspect the alignment under any viewpoint (Video 1 in Supplementary Material). Co-registration was manually performed and visually determined by an expert independent of subsequent analysis and blinded to color-coded maps of voltage and PSI (i.e. solely based on anatomical information). Emphasis was placed on the simultaneous alignment of the ascending, arch and

descending aorta, and the LV apex. No other extra-cardiac structure was systematically utilised. After co-registration, each vertex belonging to the EAM geometry (i.e. the triangular mesh produced during cardiac mapping) was paired to the closest vertex of the PSI map, provided that the Euclidean distance (D) between them was $D \leq 8$ mm.

The impact of EAM-CMR co-registration on the localization of low-voltage zones was assessed by reproducibility analysis and simulations. Intra- and inter-observer reproducibility was assessed by repeating co-registration twice (same operator, with more than 48 hours between repetitions) and by a second expert operator, respectively. Repeated co-registrations were compared by measuring the difference between the location of the aligned geometries as shifts and rotations (Euler's rule) along and about the XYZ axes. The simulation study was carried out as follows. After co-registration, small shifts and rotations were algorithmically applied to the EAM and low-voltage zones localization re-assessed. In total, the analysis was repeated 320 times per case, consistent with configurations obtained by applying simultaneous shifts and rotations of $\pm\Delta X$ mm and $\pm\Delta X°$ along and around the 3 major axes (2^6=64 configurations), where ΔX = 2°, 4°, 6°, 8° and 10°. Video 3 in Supplementary Material shows the effect of shifts and rotations of up to ±10 mm and ±10° on one representative EAM.

As the agreement between voltage and PSI is thought to be affected by each modality's spatial resolution and noise, we sought to modulate spatial resolution and reduce noise by implementing spatial smoothing. This assigns to each point in a map the average value of its neighbouring points within a given radius. Systematic variation of this radius (circular linear filters with radius equal to 2, 4 and 6 mm) allowed evaluation of the impact of spatial resolution/noise reduction on agreement between

EAM voltage and PSI. Video 2 in Supplementary Material shows the effect of increasing spatial smoothing on representative voltage and PSI maps.

Statistical analysis

Data distribution is reported as median, 1st – 3rd quartile. Correlation was assessed using the Spearman's correlation coefficient (r). Assessment of binary classification of low-voltage zones characterized by V<0.5 mV or V<1.5 mV was performed using ROC curves. The area under the ROC curve (AUC) as well as sensitivity and specificity obtained using the optimum PSI threshold (threshold corresponding to the point closest to 100 sensitivity and specificity) were estimated for each case. Sensitivity and specificity were then assessed using a fixed PSI threshold equal to the median value of case-specific PSI thresholds. EAM for which the prevalence of low-voltage zones was < 3% were not considered. Reported results represent averaged values across CMR layers spanning from sub-endocardium (layer 10%) to mid-myocardium (layer 50%) included. Results for each layer are reported in Supplementary Material.

Results

CMR scans were performed without complication in all subjects, with no significant changes in device parameters (battery voltage or lead sensitivities, thresholds or impedances) between pre- and post-CMR device interrogations. PSI scar maps were free from artefact in 3 out of the 10 patients. In the 7 remaining patients, artefacts were most frequently located at the apical cap (n=4) and on the anterior wall (n=3) (Fig. S1 in Supplementary Material). The proportion of LV surface affected by artefacts was 9.7% (1.4% – 13.9%) across patients. The median interval between CMR and electrophysiological study was 2 (5 – 23) days, with no relevant clinical events between procedures in any patient (Table 1).

Meshes of EAMs were derived from 611 (385 – 1,581) electrode points and were composed of 7,859 (6,880 – 14,952) vertices, of which 59% (48% – 65%) were paired to CMR points (Table 2), with the remaining ones often belonging to non-ventricular structures, or the valve plane or being proximal to CMR artefacts. Pooling data from all cases, the distance between CMR and EAM points was 3.36 (1.64 – 5.28) mm. Of all EAM points, 87% and 13% were collected using a Pentaray and a standard ablation catheter, respectively. In 3 cases, intracardiac electrograms were mainly collected with the ablation catheter. In two of these, all points in the EAM meshes had contact force >2 g. In the remaining case, 27% of points in the EAM mesh had either undetermined force or force < 2 g.

On CMR, end diastolic and systolic volumes were 248 (197 – 290) mL and 187 (141 – 227) mL, respectively. There was a good agreement between the area of the LV (excluding the valve plane) measured from EAM and CMR geometries, with correlation coefficient equal to r=0.879 (Supplementary Figure S8). The LV area from EAM was 0.3% (-3.5% – 7.3%) larger than LV area from CMR.

Correlation between EAM voltage and PSI

Comparison between EAM and PSI maps for 2 representative patients, including point-by-point correlations and case-specific ROC curves, is shown in Figure 1 and Figure S2 in Supplementary Material.

A significant negative correlation between bipolar voltage and PSI was registered in all patients across all cardiac sites, with a correlation coefficient equal to -0.57 (-0.68, -0.42). PSI correlation with unipolar voltage was also significant, but lower, with correlation coefficient equal to -0.49 (-0.65, -0.36). Correlation between endocardial

bipolar voltage and PSI and between endocardial unipolar voltage and PSI was not significantly different across different transmural layers, form endocardial to epicardial PSI layers (Fig. S3 in Supplementary Materials).

Agreement in LVZ localization

Case by case ROC analyses showed good localization of low-voltage zones (Table 2), with AUC for the localization of areas with V<1.5 mV of 0.82 (0.76 – 0.83), sensitivity of 74% (71% – 77%) and specificity of 78% (73% – 83%) [results shown as median (interquartile range) of case-by-case ROC analysis]. Localization of areas with V<0.5 mV was similar (Table 2). The correlation coefficient between the area of low-voltage zones from EAM and PSI maps was 0.87 for V<0.5 mV and 0.79 for V<1.5 mV (Figure 2). Agreement between CMR and EAM for localization of LVZ was similar in cases where the majority of data was collected using an ablation catheter (n=3) and where a Pentaray (n=7) catheter was used (Supplementary Table S1).

These results were obtained using case-specific ROC-derived PSI thresholds. Similar results were obtained when using a fixed PSI threshold for all cases, taken as the median value of the case-specific PSI thresholds (i.e. PSI>41% for V<1.5 mV and PSI>46% for V<0.5 mV, Table 2). Sensitivity and specificity were 71% (65%-81%) and 76% (69%-86%) for V<1.5 mV, and 79% (62%-86%) 67% (67%-77%) for V<0.5 mV, respectively.

As expected, given that voltage maps were collected on the endocardium, low-voltage zones localization was more accurate using endocardial than epicardial PSI layers (Fig. S4 in Supplementary Material). However, accuracy in low-voltage zones localization using PSI was not significantly different for the sub-endocardial as compared to mid-myocardial layer (Supplementary Fig. S4).

Across all patients, mean PSI at ablation sites was 65% (63% – 73%), and 93% (83% – 100%) of ablation sites were located in areas of scar (i.e. above PSI threshold) in PSI maps. The distribution of ablation sites mapped onto a co-registered PSI map, including electrograms recorded at a cardiac site where ablation terminated a subsequently induced VT, is shown for one case in Fig. 4.

Choosing a different minimum distance required for pairing CMR and EAM points modified the number of paired sites without significantly affecting the results (Fig. S7 in Supplementary Material). Finally, rescaling PSI values to their 5^{th} and 95^{th} percentile value instead of between minimum and maximum did not affect the results (Table 2 in Supplementary Material).

Effect of co-registration misalignments

Results of the simulation study to assess low-voltage zones localization after algorithmically altering co-registration showed that misalignments can have a strong impact on the agreement between PSI and voltage, with both PSI-voltage correlation and discrimination of low-voltage zones decreasing for increasing shifts/rotations (Figure 3A). Nevertheless, intra- and inter-operator co-registration variability had little impact on low-voltage zones localization (Figure 3B). The position of the aligned geometries after repeated co-registrations differed by few millimetres (median absolute shift along X, Y and Z axes was equal to 2.6, 2.9 and 2.3 mm, respectively) and degrees (median absolute rotation about X, Y and Z axes was equal to 4.7, 3.1, 13.3° respectively) (Supplementary Table 3). Pair-wise correlation coefficients between AUC obtained using reference and additional co-registrations ranged between 0.83 and 0.88, while intraclass correlation coefficients measuring the agreement between AUC estimates across all configurations was equal to 0.86 and

0.88 for localization of V<1.5 mV and V<0.5 mV, respectively (Fig. S5 in Supplementary Material).

Effect of spatial smoothing

Spatial smoothing gradually improved agreement between voltage and PSI maps. Maximum smoothing (R=6 mm) in both PSI and voltage resulted in an increase in median PSI-voltage correlation coefficient of 13.7% (P=0.002, Figure 3C) and in median AUC of 5.8 (P=0.004, Figure 3C) with respect to non-smoothed maps. Effect of spatial smoothing applied in isolation or in combination to PSI and voltage maps is described in detail in the Supplementary Material (Fig. S6).

Discussion

The aim of this study was to assess performance and limitations of low-voltage zones (LVZ) localisation by optimised LGE-CMR scar imaging in patients with CIEDs and co-registration algorithms for the delineation of scar in patients with CIEDs. We applied state of the art CMR imaging and electro-anatomical mapping to quantify spatial correlation between EAM voltage and PSI across all cardiac sites, focussing on the impact of co-registration and spatial resolution.

The main findings are: (1) PSI showed a significant inverse correlation with EAM voltage (r=-0.57, interquartile range -0.68, -0.42) and allowed localization of low-voltage zones with median sensitivity and specificity of 74% and 78%, (2) Small variations in EAM-CMR anatomical co-registration can worsen the localization of low-voltage zones, but the use of the ascending and descending aorta to guide co-registration ensures high intra- and inter-operator reproducibility.

With increasing numbers of patients with CIEDs considered for VT ablation due to recurrent arrhythmias and appropriate shocks, techniques are required to improve

procedural success rates whilst reducing radiation dose and procedural times. LGE-CMR can aid scar localization and pre-procedural planning (2–7,16), however CMR in patients with CIEDs has generally been avoided due to concerns related to risk and poor image quality from device-related artefact. Few studies had previously investigated EAM and CMR in patients with CIEDs. These had focused on scar size (13), feasibility (17) and correlation between critical sites for re-entry initiation (8), but localization of low-voltage zones by CMR, which is crucial for VT catheter ablation, is still undetermined. This study provides the first assessment of the agreement between voltage and PSI maps in patients with CIEDs. Importantly, it provides quantitative assessment of the impact of co-registration misalignments, which has significant implications particularly in the context of a purely anatomical scar mapping strategy to identify corridors that support re-entry (8,9). Indeed, a recent study has shown that CMR-guided catheter ablation based on localization of critical sites of VT through advance image processing of PSI maps can reduce procedural time and improve outcomes of VT catheter ablation (9). Another potential application for CMR may be in combination with other non-invasive modalities to identify ablation target for stereotactic body radiotherapy (18,19). For instance, ECG-Imaging could be used for identification of VT sites of origin and delineation of the functional electrophysiological substrate related to activation and repolarization abnormalities (14,15,20), whereas CMR could be used for scar delineation and identification of corridors supporting the VT circuit.

Impact of EAM-CMR co-registration

Co-registration usually involves minimization of the distance between landmark points, followed by manual adjustment by expert operators. This can introduce bias, particularly if only LV models are used for alignment. We assessed the impact of small

random alterations in the co-registration by algorithmically applying rotations and shifts to the EAM after co-registration. We found that these had an impact and that in some cases even small rotations and shifts considerably reduced the agreement between voltage and PSI maps. Despite this, we found that intra and inter-operator co-registration variability was low, and reproducibility of low-voltage zones localization was high (intraclass correlation of AUC equal to 0.86). This is the first study to assess the reproducibility of co-registration, which in this study was optimised by the utilization of the full 3D geometry of the ascending, arch, and descending aorta. The use of the full aortic geometry to co-register CMR and electro-anatomical data was proposed in one of the seminal studies on EAM-CMR integration (21) but has not been adopted as standard clinical practice. Previous studies have used other anatomical landmarks for co-registration, including the position of the mitral annulus, proximal aorta, pulmonary artery, RV or the ostium of the left main coronary artery (4,9) and one study has analysed the effects of rotation (but not shifts) on co-registration accuracy (22).

Methodological considerations

LGE-CMR corelates well histologically with various models of myocardial fibrosis (23) , but quantitative evaluation of LGE is challenging, with signal thresholding impacting on the projected infarct size. Despite good correlation between EAM voltage and PSI using fixed thresholds based on the median values across the cohort, the optimal PSI threshold varied considerably across cases, and there was a narrow gap between optimum thresholds for localization of low-voltage zones with V<1.5 mV and V<0.5 mV. This highlights the challenge of delineating scar border-zones (0.5 – 1.5 mV), which beyond the limitations of spatial resolution inherent to each modality may be related to the effect of wall thickness (24), catheter configuration (25) , variable CMR

contrast kinetics or residual hypersensitivity and signal void related to the presence of the ICD.

In primary analysis, we have reported averaged values across CMR layers spanning from sub-endocardium (layer 10%) to mid-myocardium (layer 50%). Layer-by-layer analysis has shown that localization of endocardial low-voltage zones was more accurate when using endocardial layers as compared to epicardial ones (Supplementary Figure S4). However, accuracy in low-voltage zones localization was not significantly different in the sub-endocardial PSI layers as compared to mid-myocardial ones. There are several possible explanations for this, predominantly driven by the limitations of the respective techniques. Whilst mid-myocardial scar may be less apparent on endocardial EAM, there are also challenges in segmenting the true endocardium with CMR and accurately demonstrating the blood-myocardial boundary. The proximity of the 10% layer to the blood pool may occasionally result in partial volume effects within the endocardial voxel which might introduce artefact in the reconstructed 3D model. Despite attempts to limit this by using thin 2D slices (4mm), in some cases this cannot be corrected. This limitation is further accentuated in cases of severe ischaemic cardiomyopathy in view of the reduced wall thickness of infarcted myocardium.

Correlation between endocardial unipolar voltage and PSI was similar across all PSI layers, including deeper mid-myocardial and sub-epicardial layer (Supplementary Figure S3). Although endocardial unipolar voltage has been shown to enable localization of epicardial scar, evidence is stronger for non-ischaemic cardiomyopathy and in absence of endocardial scar (26). Furthermore, theoretical (27) and experimental (28) studies have demonstrated that the amplitude of the unipolar electrogram is mainly determined by remote activity (and in particular by the sequence

of electrical depolarization) and therefore it is not an ideal parameter for localization of scar.

In this study, we used spatial smoothing to reduce noise in both voltage and PSI maps. Spatial smoothing improved agreement between voltage and PSI maps with moderate but significant increase in voltage-PSI correlation and low-voltage zone discrimination. However, since smoothing reduces spatial resolution, its use may be limited to the localization of large areas of scar as opposed to the fine details of the scar architecture.

Limitations

Our study is limited by the small sample size. However, patients had high-density EAM and complete geometry of the aorta, which is crucial to ensure detailed delineation of the substrate and optimal co-registration. EAM was used as a reference for the identification of abnormal tissue, and although Pentaray was used to collect most points, an ablation catheter was occasionally used. Bipolar voltage can be affected by wave-front directionality and catheter configuration (25). Although higher spatial resolution LGE imaging can be obtained using 3D MRI ($1.9\times1.9\times1.9$ mm^3), 3D wideband LGE imaging is generally unfeasible in patients with frequent ventricular arrhythmias awaiting ablation. Finally, this study was limited to endocardial maps and did not focus on the utility of integrating CMR with EAM data during catheter ablations (6–8). This however should be the focus of further investigation.

Conclusions

In patients with CIEDs, use of novel wideband CMR LGE sequences and strategies to optimize co-registration can localize areas of scar with good accuracy. To fully establish the role of CMR in assisting VT ablation, effort should be focused on

standardising co-registration, improving data acquisition and reducing noise in both modalities.

Perspectives

Competency in medical knowledge: This study shows that optimised cardiac MRI enables non-invasive localization of scar in patients with cardiac implantable electronic devices and it highlights the importance of using the thoracic aorta as a landmark for accurate co-registration with electro-anatomical maps.

Translational outlook: Optimised MRI sequences and accurate co-registration of cardiac MRI scar maps with electro-anatomical geometries could improve VT ablation.

References

1. Graham AJ., Orini M., Lambiase PD. Limitations and challenges in mapping ventricular tachycardia: New technologies and future directions. Arrhythmia Electrophysiol Rev 2017;6(3):118–24. Doi: 10.15420/aer.2017.20.1.

2. Ashikaga H., Sasano T., Dong J., et al. Magnetic resonance-based anatomical analysis of scar-related ventricular tachycardia: Implications for catheter ablation. Circ Res 2007;101(9):939–47. Doi: 10.1161/CIRCRESAHA.107.158980.

3. Codreanu A., Odille F., Aliot E., et al. Electroanatomic Characterization of Post-Infarct Scars: Comparison With 3-Dimensional Myocardial Scar Reconstruction Based on Magnetic Resonance Imaging. J Am Coll Cardiol 2008;52(10):839–

42. Doi: 10.1016/J.JACC.2008.05.038.

4. Wijnmaalen AP., Van Der Geest RJ., Van Huls Van Taxis CFB., et al. Head-to-head comparison of contrast-enhanced magnetic resonance imaging and electroanatomical voltage mapping to assess post-infarct scar characteristics in patients with ventricular tachycardias: Real-time image integration and reversed registration. Eur Heart J 2011;32(1):104–14. Doi: 10.1093/eurheartj/ehq345.

5. Sramko M., Hoogendoorn JC., Glashan CA., Zeppenfeld K. Advancement in cardiac imaging for treatment of ventricular arrhythmias in structural heart disease. Europace 2019;21(3):383–403. Doi: 10.1093/europace/euy150.

6. Andreu D., Berruezo A., Ortiz-Pérez JT., et al. Integration of 3D electroanatomic maps and magnetic resonance scar characterization into the navigation system to guide ventricular tachycardia ablation. Circ Arrhythmia Electrophysiol 2011;4(5):674–83. Doi: 10.1161/CIRCEP.111.961946.

7. Andreu D., Penela D., Acosta J., et al. Cardiac magnetic resonance–aided scar dechanneling: Influence on acute and long-term outcomes. Heart Rhythm 2017;14(8):1121–8. Doi: 10.1016/j.hrthm.2017.05.018.

8. Roca-Luque I., Van Breukelen A., Alarcon F., et al. Ventricular scar channel entrances identified by new wideband cardiac magnetic resonance sequence to guide ventricular tachycardia ablation in patients with cardiac defibrillators. Europace 2020;22(4):598–606. Doi: 10.1093/europace/euaa021.

9. Soto-Iglesias D., Penela D., Jáuregui B., et al. Cardiac Magnetic Resonance-Guided Ventricular Tachycardia Substrate Ablation. JACC Clin Electrophysiol 2020;6(4):436–47. Doi: 10.1016/j.jacep.2019.11.004.

10. Bhuva AN., Kellman P., Graham A., et al. Clinical impact of cardiovascular magnetic resonance with optimized myocardial scar detection in patients with cardiac implantable devices. Int J Cardiol 2019;279:72–8. Doi: 10.1016/j.ijcard.2019.01.005.

11. Seewöster T., Löbe S., Hilbert S., et al. Cardiovascular magnetic resonance imaging in patients with cardiac implantable electronic devices: best practice and real-world experience. Europace 2019;21(8):1220–8. Doi: 10.1093/europace/euz112.

12. Dickfeld T., Tian J., Ahmad G., et al. MRI-guided ventricular tachycardia ablation integration of late gadolinium-enhanced 3D scar in patients with implantable cardioverter- defibrillators. Circ Arrhythmia Electrophysiol 2011;4(2):172–84. Doi: 10.1161/CIRCEP.110.958744.

13. Stevens SM., Tung R., Rashid S., et al. Device artifact reduction for magnetic resonance imaging of patients with implantable cardioverter-defibrillators and ventricular tachycardia: Late gadolinium enhancement correlation with electroanatomic mapping. Heart Rhythm 2014;11(2):289–98. Doi: 10.1016/j.hrthm.2013.10.032.

14. Graham AJ., Orini M., Zacur E., et al. Simultaneous Comparison of Electrocardiographic Imaging and Epicardial Contact Mapping in Structural Heart Disease. Circ Arrhythmia Electrophysiol 2019;12(4):e007120. Doi: 10.1161/CIRCEP.118.007120.

15. Graham AJ., Orini M., Zacur E., et al. Evaluation of ECG Imaging to Map Haemodynamically Stable and Unstable Ventricular Arrhythmias. Circ Arrhythmia Electrophysiol 2020. Doi: 10.1161/circep.119.007377.

16. Desjardins B., Crawford T., Good E., et al. Infarct architecture and characteristics on delayed enhanced magnetic resonance imaging and electroanatomic mapping in patients with postinfarction ventricular arrhythmia. Heart Rhythm 2009;6(5):644–51. Doi: 10.1016/j.hrthm.2009.02.018.

17. Singh A., Kawaji K., Goyal N., et al. Feasibility of Cardiac Magnetic Resonance Wideband Protocol in Patients With Implantable Cardioverter Defibrillators and Its Utility for Defining Scar. Am J Cardiol 2019;123(8):1329–35. Doi: 10.1016/j.amjcard.2019.01.018.

18. Robinson CG., Samson PP., Moore KMS., et al. Phase I/II Trial of Electrophysiology-Guided Noninvasive Cardiac Radioablation for Ventricular Tachycardia. Circulation 2019;139(3):313–21. Doi: 10.1161/CIRCULATIONAHA.118.038261.

19. Cuculich PS., Schill MR., Kashani R., et al. Noninvasive Cardiac Radiation for Ablation of Ventricular Tachycardia. N Engl J Med 2017;377(24):2325–36. Doi: 10.1056/nejmoa1613773.

20. Wang Y., Cuculich PS., Zhang J., et al. Noninvasive Electroanatomic Mapping of Human Ventricular Arrhythmias with Electrocardiographic Imaging. Sci Transl Med 2011;3(98):98ra84-98ra84. Doi: 10.1126/scitranslmed.3002152.

21. Reddy VY., Malchano ZJ., Holmvang G., et al. Integration of cardiac magnetic resonance imaging with three-dimensional electroanatomic mapping to guide left ventricular catheter manipulation: Feasibility in a porcine model of healed myocardial infarction. J Am Coll Cardiol 2004;44(11):2202–13. Doi: 10.1016/j.jacc.2004.08.063.

22. Tao Q., Milles J., Van Huls Van Taxis C., et al. Toward magnetic resonance-

guided electroanatomical voltage mapping for catheter ablation of scar-related ventricular tachycardia: A comparison of registration methods. J Cardiovasc Electrophysiol 2012;23(1):74–80. Doi: 10.1111/j.1540-8167.2011.02167.x.

23. Iles LM., Ellims AH., Llewellyn H., et al. Histological validation of cardiac magnetic resonance analysis of regional and diffuse interstitial myocardial fibrosis. Eur Heart J Cardiovasc Imaging 2015;16(1):14–22. Doi: 10.1093/ehjci/jeu182.

24. Glashan CA., Androulakis AFA., Tao Q., et al. Whole human heart histology to validate electroanatomical voltage mapping in patients with non-ischaemic cardiomyopathy and ventricular tachycardia. Eur Heart J 2018;39(31):2867–75. Doi: 10.1093/eurheartj/ehy168.

25. Takigawa M., Relan J., Kitamura T., et al. Impact of Spacing and Orientation on the Scar Threshold With a High-Density Grid Catheter. Circ Arrhythmia Electrophysiol 2019;12(9):e007158. Doi: 10.1161/CIRCEP.119.007158.

26. Hutchinson MD., Gerstenfeld EP., Desjardins B., et al. Endocardial unipolar voltage mapping to detect epicardial ventricular tachycardia substrate in patients with nonischemic left ventricular cardiomyopathy. Circ Arrhythmia Electrophysiol 2011;4(1):49–55. Doi: 10.1161/CIRCEP.110.959957.

27. Potse M., Vinet A., Opthof T., Coronel R. Validation of a simple model for the morphology of the T wave in unipolar electrograms. Am J Physiol Heart Circ Physiol 2009;297(2):H792–801. Doi: 10.1152/ajpheart.00064.2009.

28. Orini M., Taggart P., Lambiase PD. In vivo human sock-mapping validation of a simple model that explains unipolar electrogram morphology in relation to conduction-repolarization dynamics. J Cardiovasc Electrophysiol

2018;29(7):990–7. Doi: 10.1111/jce.13606.

Figures

Figure 1.

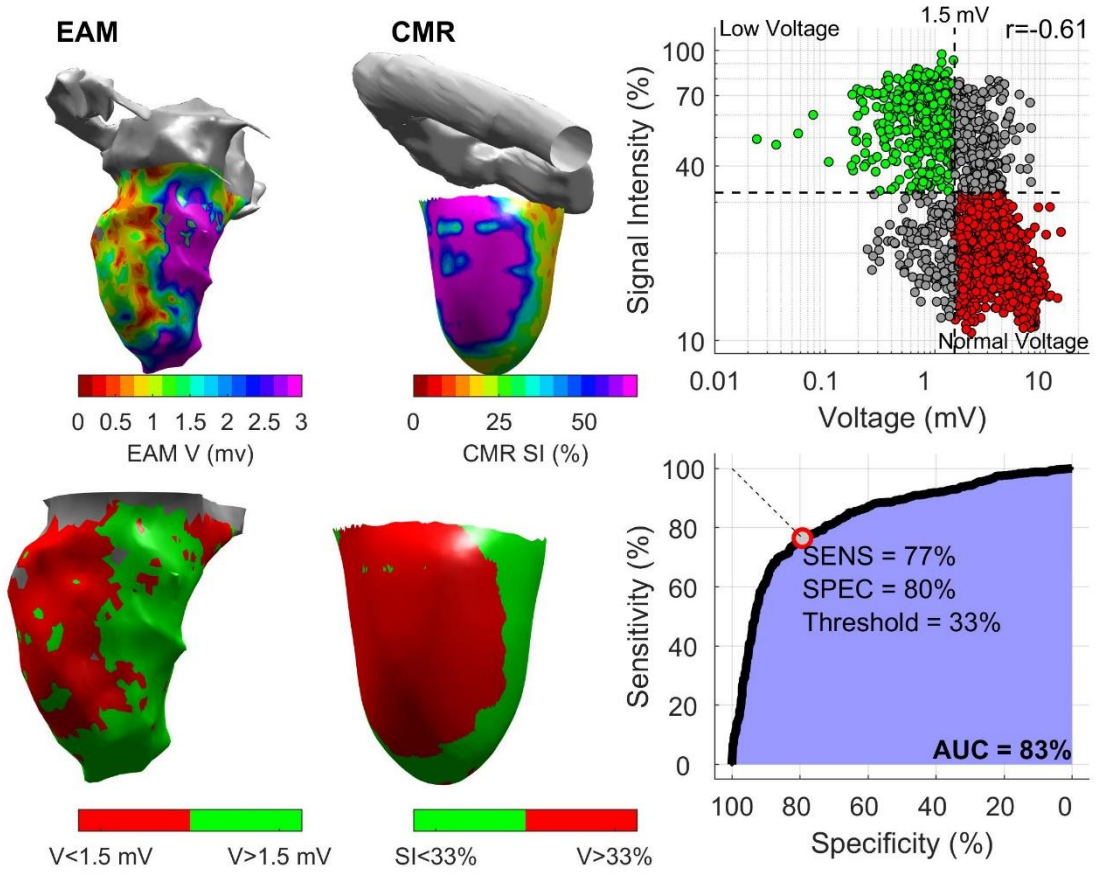

Figure 1: **Comparison between EAM and LGE-CMR (example Subject #9)**. Top: voltage and CMR-intensity maps (3D transmurality) shown side-by-side. Bottom: Low-voltage areas (V<1.5 mV) and areas with PSI>33% indicating abnormal tissue are shown on the left and right, respectively. Maps from left to right are shown in the same reference system. Top-right inset shows correlation between voltage and PSI (on loglog scale), with green representing true positives and red representing true

negative. Correlation coefficient was r=-0.61. Bottom-right inset shows ROC curve with a circle representing optimal threshold for identification of low-voltage zones. EAM: Electroanatomical map. LGE-CMR: Late gadolinium enhancement cardiovascular magnetic resonance. AUC: Area under the ROC curve.

Figure 2.

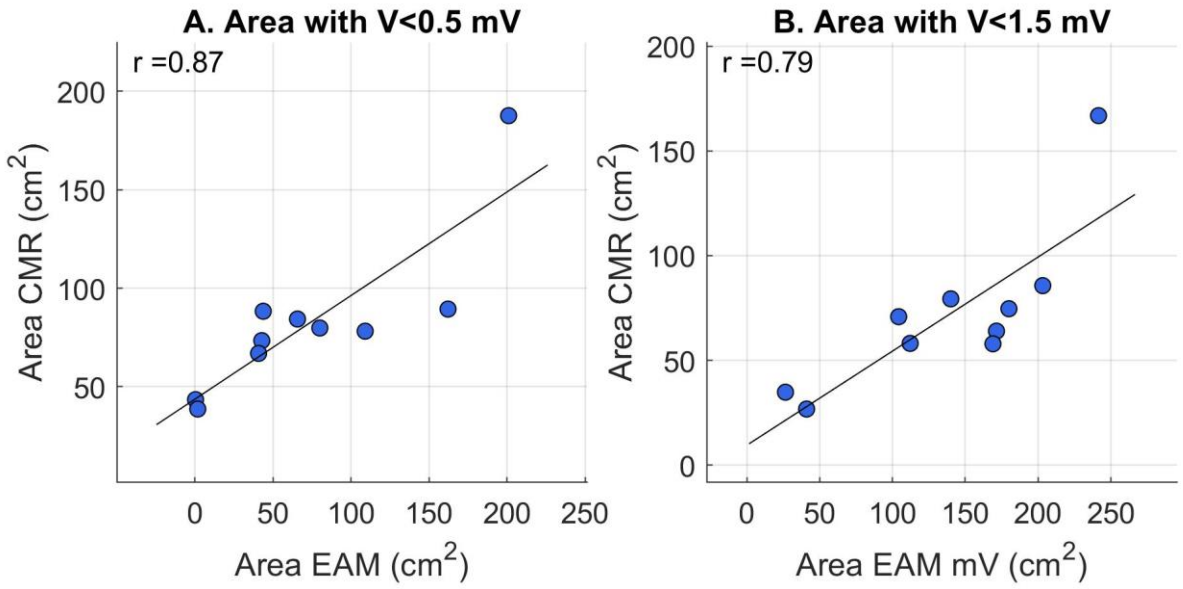

Figure 2: Correlation between scar area on EAM and CMR-LGE. Linear fitting is reported with a solid line and correlation coefficient (r) is shown on the top-left corner. On EAM, low-voltage zones were defined with V<0.5 mV and V<1.5 mV. On CMR maps, areas representing low-voltage zones were identified with case-specific thresholds obtained through ROC analysis (average of layers spanning from sub-endocardium, layer 10, to mid-myocardium, layer 50).

Figure 3.

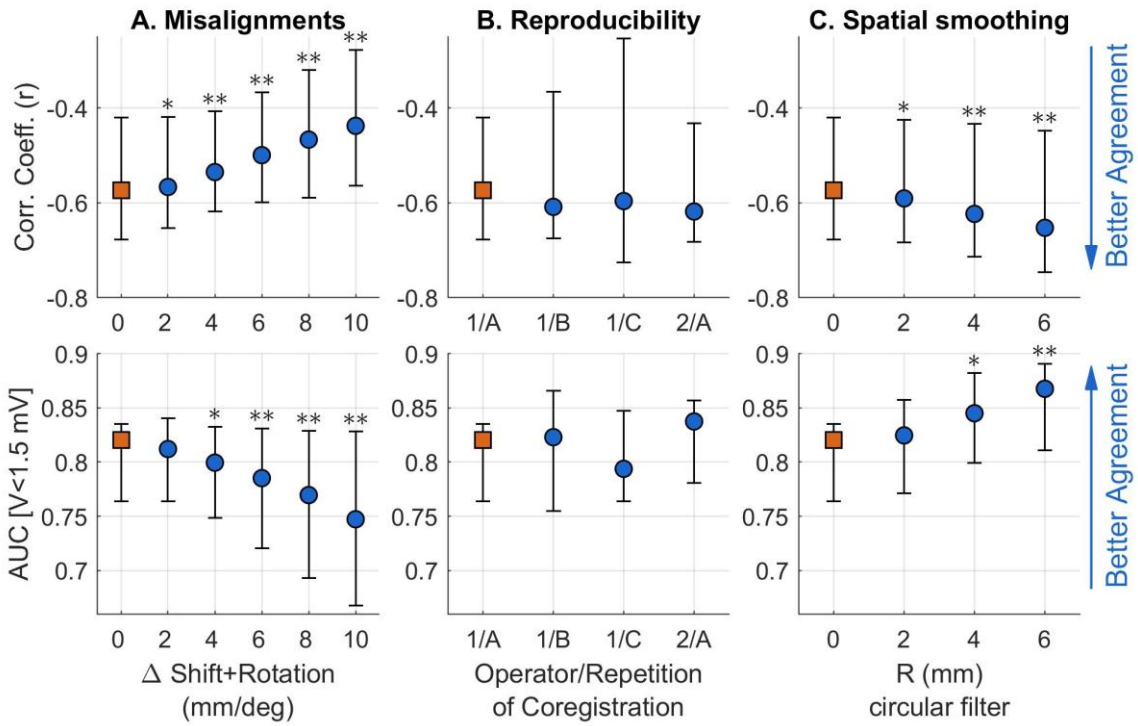

Figure 3: EAM-CMR agreement. Effect of misalignment in co-registration (A), inter- and intra-operator variability of co-registration (B) and spatial smoothing of voltage and pixel intensity signal (PSI) maps (C) on EAM-CMR agreement. A: Expert-based co-registration of each case was algorithmically modified by simultaneously shifting (*Δ* mm) and rotating (*Δ* deg) the voltage map along and across the 3 orthogonal axes (64 iteration per *Δ* and patient). B: EAM and voltage maps were co-registered by a first operator three times (1A, 1B and 1C) and by a second operator (2A). C: Increasing degree of spatial smoothing of voltage and PSI maps using a circular filter of radius equal to 2, 4 and 6 mm. Markers and whiskers represent median value and interquartile range. r: Spearman's correlation coefficient between PSI and voltage across cardiac sites. AUC: Area under the ROC curve for localization of zones with V<1.5 mV. * P<0.05; ** P<0.005 (Wilcoxon signed-rank test) with respect to reference values (red squares, corresponding to Δ=0 in A; 1A in B; R=0 in C).

Figure 4

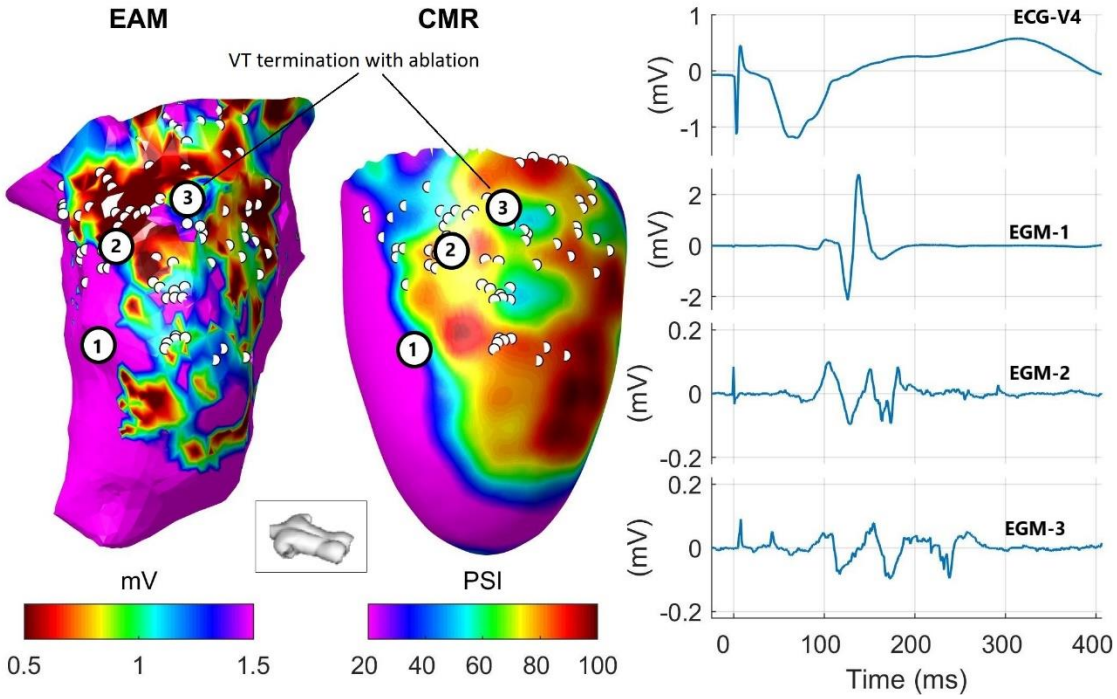

Figure 4: VT critical sites on EAM and CMR-PSI. Left: Electro-anatomical map (EAM) collected while pacing from the RV apex and CMR pixel signal intensity (PSI) map (endocardial layer corresponding to 10% of wall thickness). White dots indicate ablation sites projected onto the two geometries. Electrograms (EGM) from sites labelled 1 (healthy tissue), 2 (dense scar) and 3 (VT exit site) are shown on the right as EGM-1,2 and 3. Ablation proximal to site 3 terminated ventricular tachycardia induced after substrate mapping. Note y-scale is adjusted to the signal's amplitude.

Tables

Table 1

ID	Sex (M/F)	Age (years)	Aetiology	Type of Device	MR Conditional	LVEF (%)	Artefacts (% of myocardium)	Interval CMR-ablation (weeks)	First/ Redo Ablation
1	M	68	IHD	CRTD	No	52	13.9	0.3	First
2	M	69	IHD	ICD	Yes	34	1.4	44.3	First
3	M	79	IHD	CRTD	No	16	0.0	0.9	Redo
4	M	84	IHD	ICD	No	19	9.7	4.0	First
5	F	79	IHD	ICD	Yes	20	9.8	0.6	First
6	M	84	IHD	ICD	No	25	10.2	0.0	First
7	M	78	IHD	CRTD	Yes	10	8.8	0.0	Redo
8	M	56	DCM	CRTD	No	20	28.9	0.3	First
9	M	73	IHD	ICD	Yes	41	0.2	8.3	First
10	M	72	IHD	CRTD	Yes	23	25.9	1.0	First

Table 1: Baseline demographics, clinical and CMR data of the patient cohort.

CMR-EP interval: time delay between CMR and VT ablation.

Table 2

	Points			V<0.5 mV					V<1.5 mV				
Patient number	**EAM Mesh**	**Paired (%)**	**Corr. Coeff.**	**PREV (%)**	**AUC**	**THR (%)**	**SENS (%)**	**SPEC (%)**	**PREV (%)**	**AUC (%)**	**THR (%)**	**SENS (%)**	**SPEC (%)**
1	3,871	58	-0.54	1	-	-	-	-	22	0.76	50	74	71
2	22,669	83	-0.32	22	0.58	35	64	54	55	0.70	33	68	67
3	7,947	48	-0.68	35	0.87	46	83	77	63	0.83	42	73	79
4	7,770	43	-0.69	22	0.83	50	83	72	62	0.87	41	78	83
5	6,880	65	-0.42	30	0.77	51	80	72	56	0.69	47	64	73
6	14,952	55	-0.50	49	0.80	41	72	76	76	0.81	37	71	78
7	15,583	41	-0.73	54	0.91	53	85	87	72	0.87	46	76	86
8	8,896	61	-0.61	22	0.79	49	78	69	44	0.83	44	80	76
9	2,438	88	-0.61	5	0.75	38	81	66	36	0.83	33	77	80
10	7,674	60	-0.31	80	0.69	36	77	60	96	0.79	33	75	84
Median	**7,859**	**59**	**-0.57**	**26**	**0.79**	**46**	**80**	**72**	**59**	**0.82**	**41**	**74**	**78**
Q1	6,880	48	-0.68	22	0.73	37	76	65	44	0.76	33	71	73
Q3	14,952	65	-0.42	49	0.84	51	83	76	72	0.83	46	77	83

Table 2: Low-voltage zone localization. EAM: Electroanatomical map. MED: Median. Q1 and Q3: First and third quartile, respectively. PREV: Prevalence of LVZ across paired points. AUC: Area under the ROC curve. THR: PSI Case-specific threshold. SENS: Sensitivity. SPEC: Specificity.